S- and P-wave velocity model estimation from seismic surface-waves.

Farbod Khosro Anjom[1], Frank Adler[2], Laura Valentina Socco[1]

[1]Department of Environment, Land and Infrastructure Engineering, Politecnico di Torino, Turin, 10128, Italy
[2] CSTJF, TotalEnergies, Pau, 64000, France

5   *Correspondence to*: Farbod Khosro Anjom (Khosro-Anjom.Farbod@polito.it)

Abstract. The surface-waves methods are well-established techniques for subsurface S-wave velocity (VS) reconstruction. Recently, the sensitivity of surface-wave skin depth to Poisson ratio was applied to also estimate P-wave velocity (VP) models from surface-wave records. We use this technique within the framework of three surface-wave methods, the wavelength/depth data transform, the laterally constrained inversion, and surface-wave tomography to estimate both VS and VP models. We

10   apply these methods to a 3-D test data set from a mining site that is characterized by stiff material and by significant elevation contrast. The data were recorded using a regular grid of receivers and an irregular source layout. Pseudo 3D VS and VP models were obtained down to 140 m depth over approximately 900×1500 m^2 area. The estimated models from the methods well-match the geological information available for the site. Less than 6% difference is observed between the estimated VS models from the three methods, whereas this value is 7.1% for the retrieved VP models. The different methods are critically compared

15   in terms of resolution and efficiency.

1 Introduction

Surface-wave methods are powerful tools for subsurface characterization. Most of these methods process the data to extract the surface-wave dispersion curve (DC) from seismic records and invert these DCs to estimate the velocity models. Since the energy decay of surface-waves wavefield in depth depends on their wavelength, the investigation depth of the surface-wave

20   methods is related to the maximum recovered wavelength and can be considerably variable, ranging from a few metres (e.g., Xia et al., 2002; Feng et al., 2004; Comina et al., 2011; Pan et al., 2018) to several tens of metres (e.g., Mordret et al., 2014; Da col et al., 2019) or even to a few kilometres (e.g., Ritzwoller and Levshin, 1998; Kennet and Yoshizawa, 2002; Fang et al., 2015). The estimated models from surface-wave techniques can be used in many applications such as near-surface site characterization (Lai, 1998; Foti et al., 2015; Garofalo et al., 2016), static corrections (Mari, 1984; Roy et al., 2010;

25   Papadopoulou et al., 2020), and ground roll prediction and damping (Blonk and Herman, 1994; Ernst et al., 2002; Halliday et al., 2010).

Different methods can be adopted for extracting DCs from the seismic records and invert them. Papadopoulou (2021) provided a thorough review of the different processing techniques and characteristics of the estimated DCs. The retrieval of a velocity model from the DC can be based on simple data transformations or on model optimization approaches with different inversion

30   strategies. According to the chosen workflow the computational cost and model resolution may vary and identifying the

optimal approach for the analysis is an important task. Here, we compare three different methods (wavelength/depth data transform, laterally constrained inversion, and surface-wave tomography) and apply them on a challenging dataset.

Regardless of the type of the surface-wave technique, since DCs are known to have lower sensitivity to P-wave velocity (VP) compared to VS, most surface-wave methods focus on VS estimation, and they require *a priori* Poisson's ratio or VP for the
35   inversion stage. Recently, a data transformation method based on the so-called wavelength-depth (W/D) relationship was developed to estimate both VS and VP models (Khosro Anjom et al., 2019). The W/D relationship is obtained by computing wavelength - depth couples corresponding to equal phase-velocity of surface-waves and time-average VS and represents the skin depth of SW Socco et al. (2017). Once estimated, the W/D relationship can be used to directly estimate time-average VS velocity from DCs. Socco and Comina (2017) showed with synthetic and real tests that the W/D relationship is highly sensitive
40   to Poisson's ratio, and it can be used to estimate time-average VP. Khosro Anjom et al. (2019) developed a data-driven W/D workflow that directly estimates interval VS and VP models from the DCs and is valid for sites with significant lateral variations. The method also provides the Poisson's ratio, which can be considered *a priori* in other surface-wave methods, such as laterally constrained inversion (LCI) and surface-wave tomography (SWT).

The earliest applications of LCI were on resistivity data (Auken and Christiensen, 2004; Wisén et al., 2005; Auken et al.,
45   2005). The first successful application of the LCI to surface-waves was performed by Wisén and Christiansen (2005). In LCI, several multi-channel DCs available along a line or over an area are associated with local relevant 1D models and inverted simultaneously. The parameters of the 1D models are connected laterally and vertically through a set of constraints, whose strength controls the variations between model parameters in adjacent model points (Boiero and Socco 2010). As a result, consistent and smooth estimated pseudo 2-D or 3-D models are usually obtained from the LCI applications.

50   In the context of earthquake seismology, SWT is a well-stablished method for VS reconstruction of the crust and upper mantel (Wespestad et al., 2019; Bao et al., 2015; Boiero, 2009; Yao et al., 2008; Shapiro et al., 2005). Recently, a few authors showed the application of SWT for the near-surface characterization, using active (Da Col et al., 2019; Socco et al., 2014; Khosro Anjom et al., 2021) and passive data (Badal et al., 2013; Picozzi et al., 2009; Colombero et al., 2022).

In literature, DC estimation methods are usually categorized into multi-channel and two-station methods, even though there
55   are no theoretical and significant technical differences between the two approaches (Papadopoulou, 2021). The multi-channel technique is the most common approach, in which the recordings from an array of receivers (in 2-D scheme) go through a wavefield transform (e.g., *f-k*, *f-v* and *τ-p*) and the DC is picked on the spectrum as the local maxima within the frequency band of surface-waves. The multi-channel processing stage is repeated to estimate DCs at different locations, which are then inverted individually (e.g., fast simulated annealing of Beaty et al., 2002) or simultaneously (e.g., LCI of Socco et al., 2009) to estimate
60   S-wave velocity (VS) model. For SWT, DC are estimated using the two-station processing method, in which the recordings of receiver couples aligned with sources are considered to estimate many path-averaged DCs that are later inverted using a tomographic scheme to estimate directly (Boschi and Ekstrom, 2002; Fang et al., 2015; Boiero, 2009; Socco et al., 2014; Karimpour et al., 2022) or indirectly (Yoshizawa and Kennett, 2004; Shapiro and Ritzwoller, 2002; Yao et al., 2008) the VS model.

65 Here, we show the application of the three surface-wave methods, (W/D, LCI, and SWT), to estimate both VS and VP models. The first two methods are based on multichannel DCs, whereas the latter relies on two-station ones. We apply the methods to a challenging test data set that was acquired in a hard-rock environment. The data were recorded using regular grids of receivers and sources located along roads and accessible locations. This acquisition scheme, also known as carpet recording (Lys et al., 2018), creates irregular source-receiver layout that limits the use of conventional multi-channel processing methods.

70 Conversely, the irregular source-receiver geometry allows the estimation of many two-station DCs with different azimuthal angles, providing high data coverage and uniform azimuthal distribution of the paths that is in advantage of SWT.

In this paper, we first introduce the site and outline the acquisition. Then, we briefly describe the W/D, LCI and SWT techniques and show their application to the data set. We use the W/D method to estimate the *a priori* Poisson's ratio required by LCI and SWT methods, which we then employ to transform their VS results into VP. Finally, we compare the estimated

75 models and the obtained resolution from the application of each method and compare the methods from an efficiency point of view.

2 Site description

The data were acquired in a mining site in the province of Aurignac in south of France (Fig. 1a). In Fig. 1b, we show the satellite view of the site superimposed with the elevation map of the area. From north-west to south-east, a significant natural

80 and human-made elevation contrast is present. In Fig. 1c, we show the geological map of the area from the website of French geological survey (BRGM). The eastern and northern part of the site are characterized by stiff formations, mainly of limestone and marl. In the western zone, recent loose deposits are present, creating a significant lateral variation between the east and west of the site.
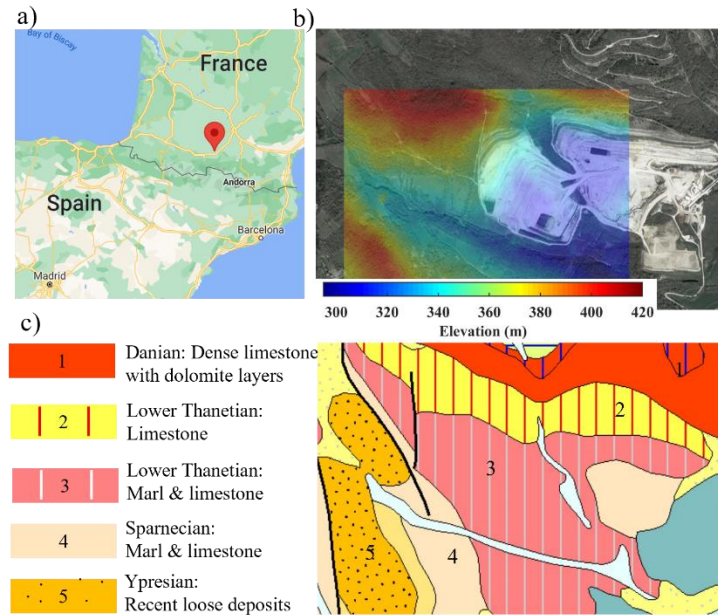
Figure 1: (a) Google map showing the location of the site (© Google Map). (b) Satellite view of the site obtained superimposed with the elevation map of the area (© Google Earth). (c) The geological map of the area obtained from French geological Survey (© BRGM - www.infoterre.brgm.fr).

3 Experimental data

The acquisition was performed inside and outside the two active open mining pits. 918 receivers were deployed within regular grids (area of 1.7 km × 1 km), and several source points (1077) were considered along the access roads, resulting in a 3-D large-scale acquisition layout. Two Birdwagen Mark IV off-road equipped with 24-ton vibrator were used as the source. The vibration included a sweep of 24 s (3 to 110 Hz) with 5 second listening time. The data were collected in real-time using RT2 wireless system. In this study, we consider a portion of the data that were collected outside the mining pits. The full description of the acquisition parameters corresponding to this portion of the data is given in Table 1.

Table 1: Acquisition parameters of the data set for outside the mining pits.

Receivers	Sources	Number of receivers	Number of shots	Sampling rate (ms)	Recording time window (s)
5 Hz vertical geophones	Vibroseis truck	581 (spacing 25 and 50 m)	533 (irregular layout)	2	5

To minimize the effect of elevation contrast (Fig. 1b), we split the data into two sub data sets (north and south), each

100   corresponding to an area with relatively flat topography. In Fig. 2, we show the acquisition layout, where different colours are

used for each sub data set.
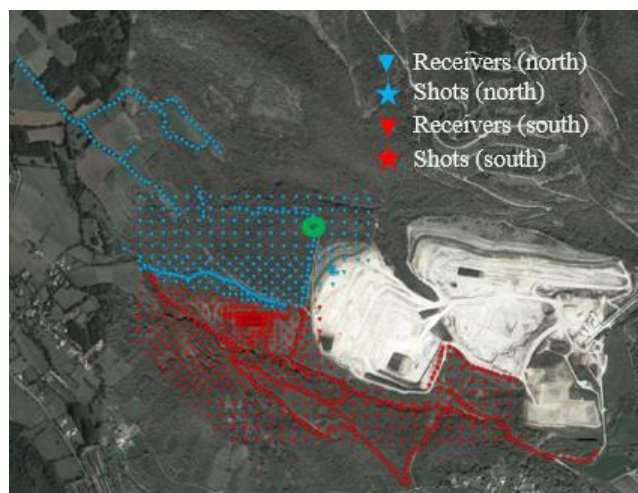
Figure 2: The satellite view of the Aurignac site (© Google Earth) superimposed with the acquisition layout. The data divided into two sub data sets shown with different colours, each within relatively flat area. The recordings from the highlighted shot (green circle) are plotted in
105   Fig. 3.

In Fig. 3, we show the first 2 s of the recordings from the highlighted source in Fig. 2 in offset domain; only 20 % of the traces

are shown for better visualization.
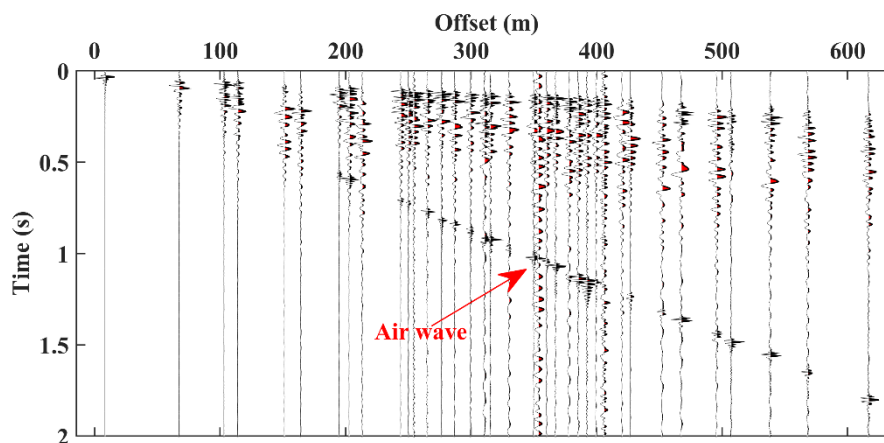
Figure 3: An example seismogram from the north zone of the Aurignac site. The shot location is highlighted with green circle in Fig. 2.

4 W/D data transform

4.1 Multi-channel processing of 3-D data

To minimize the impact of lateral variability on the DC estimation of the 3D data, we considered the recordings from receiver spread over an area (Wang et al., 2015; Xia et al., 2009; Park, 2019). For each DC estimation, we selected the receivers inside a square area (window) of 100×100 m^2 and considered the recordings from sources within a 250 m distance from the centre of the square (Fig. 4a). We used the phase-shift method (Park et al., 1998) to estimate the *f-v* spectrum. We stacked the spectra corresponding to the recordings of the same receivers but from different source locations to increase the signal-to-noise ratio (Neducza, 2007). Then, the fundamental mode was picked as the maxima on the spectrum and was assigned to the centre of the receiver spread (Fig. 4b). We shifted the window by one inter receiver spacing (50 m in the northern side and 25 m in the southern part) to estimate DCs corresponding to different locations of the site. In Fig. 4, we show an example of the DC picking for the north zone. In Fig. 4a, the 9 selected receivers inside the square are shown in blue, and the selected shots are presented in green asterisks. In Fig. 4b, we show the computed spectrum and the picked DC.
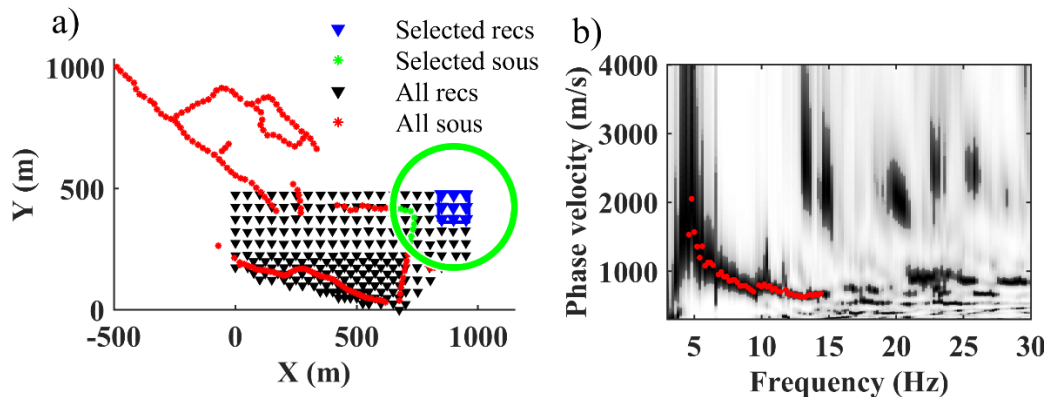
Figure 4: Example DC picking from the north zone of the site by applying phase-shift method to the recordings of receiver over the square window. (a) The geometry of the selected receivers inside the blue rectangle. The green circle shows the distance limit of the shot location (250 m) from the centre of the selected receivers. (b) Computed spectrum and picked DC in red.

4.2 W/D data transformation

The proposed method as described in Khosro Anjom et al. (2021) is composed of four main steps: (i) The clustering of DCs, (ii) selection of reference DC for each cluster and estimation of the corresponding time-average VS velocity model, (iii) the W/D relationship and apparent Poisson's ratio estimation for the reference DC of each cluster, and (iv) direct transformation of the DCs into time-average and then interval VS and VP model.

Since the same W/D relationship is applied to different DCs to transform them into velocity models, to apply the method at sites with significant lateral variations, the DCs must be clustered into more homogenous sets, and one W/D relationship should

be estimated and applied separately to each group of DCs. We use the hierarchical clustering algorithm developed by Khosro

135   Anjom et al (2017) to cluster the DCs.

In total, we estimated 545 fundamental mode DCs. In Fig. 5a, we show the estimated DCs as a function of frequency with the colour scale based on the clustering of the DCs in Fig. 5b. The DCs of the western cluster (cluster A, shown in blue in Fig. 5a) present lower phase-velocities compared to the eastern DCs (cluster B, shown in green in Fig. 5a).
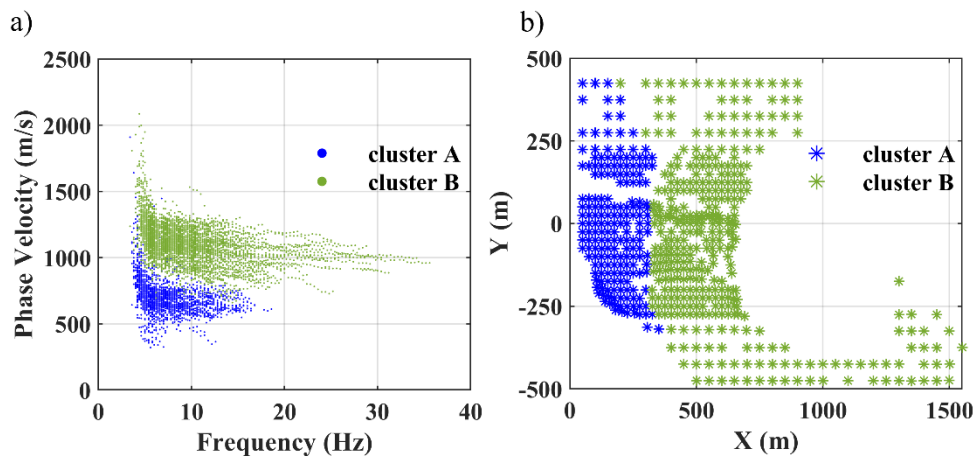
140   **Figure 5:** Multi-channel analysis of the data. (a) The estimated DCs. (b) The spatial view of the estimated DCs and obtained clusters.

For each cluster, a reference DC and its corresponding time-average VS model is needed to estimate the W/D relationship. The reference DC is selected based on the quality control proposed by Karimpour (2018). To estimate the required time-average VS model, we invert the reference DC using an optimized Monte Carlo inversion (Socco and Boiero, 2008). Among the model parameters, density is considered *a priori*, whereas VS, Poisson's ratio and thicknesses are uniformly sampled

145   within the boundaries of a wide model space. After the inversion, the accepted models are selected according to a statistical Fisher test. Unlike deterministic inversions that result in a single output, the Monte Carlo inversion leads to a set of possible solutions. We first compute time-average VS model from the VS layered models as $VS_z = \frac{\sum_n h_i}{\sum_n \frac{h_i}{VS_i}}$, where h and n are the layers thickness and total number of layers. Then, we average the values of the time-average models of the accepted model population at each depth to obtain a unique time-average VS model corresponding to the reference DC. Next, we collect the wavelength-

150   depth relationship (W/D relationship) that consists of the pairs of wavelength and depth values for which the phase velocity of the DC and the time-average VS of the MC solution have the same value. The experimental W/D relationship is significantly sensitive to Poisson's ratio. We use the method of Socco and Comina (2017) to estimate from the experimental W/D relationship an apparent Poisson's ratio that relates the time-average VS and time-average VP: First, we generate synthetic DCs corresponding to the estimated VS model from the Monte Carlo inversion and different Poisson's ratios. Then, we

155   consider these DCs and the time-average VS to retrieve synthetic W/D relationships that are each corresponding to a specific

Poisson's ratio value. Next, we deduce an apparent Poisson's ratio at each depth by comparing the experimental W/D relationship with the synthetic ones.

We use the estimated experimental W/D relationship to directly transform all DCs of the cluster into time-average VS models. Then, we transform the estimated time-average VS models into time-average VP through the estimated apparent Poisson's
160 ratio. The time-average velocities can be transformed to interval velocities using a DIX-type equation. To mitigate the effect of noise in the data, we use the regularized DIX-type formulation proposed by Khosro Anjom (2019) to transform the time-average VS and VP models to interval VS and VP. Finally, we assemble all the estimated models from the clusters to build pseudo 2-D/3-D model. Given the W/D method provides both VS and VP models, we use the estimated models at the reference location to retrieve a Poisson's ratio corresponding to the area covered by the cluster. The estimated Poisson's ratios will then
165 be used a priori in the reference model of the LCI and SWT.

In Fig. 6 and 7, we show the steps of estimating the reference W/D relationship and apparent Poisson's ratio for the reference DCs of cluster A (Fig. 6a) and B (Fig. 7a). We considered variable Poisson's ratios between 0.1 and 0.45 for the Monte Carlo inversion. We used density of 2000 kg/m3 for the first layer and constant density of 2200 kg/m3 for the other layers. We imposed a 0.05 level of confidence for the Fisher test to accept the best-fitting models among 1,000,000 sampled models. In
170 Fig. 6b and c, as well as Fig. 6b and c, we show the estimated VS and time-average VS models for cluster A and B, respectively. The estimated W/D relationship for cluster A and B are given in Fig. 6d and 7d, while the obtained apparent Poisson's ratios are provided in Fig. 6e and 7e. In Fig. 6d and e, as well as Fig. 7d and e, we also show the uncertainty associated with the reference W/D and apparent Poisson's ratio of the clusters, which was obtained based on the method of Khosro Anjom et al. (2019).

175 For both clusters, the W/D relationship and apparent Poisson's ratio were not available for the first 20 m due to the lack of short wavelength data in the experimental DCs. The investigation depth of 128 m was reached for cluster A, whereas this value was increased to 140 m for cluster B.
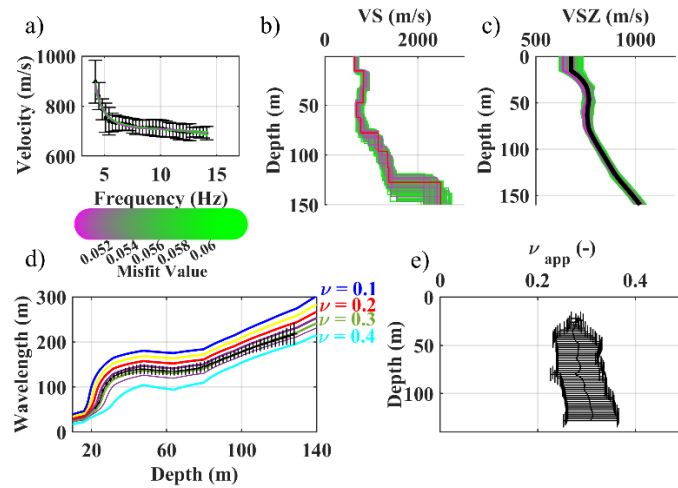
Figure 6: The steps of estimating the reference W/D relationship and apparent Poisson's ratio for cluster A. (a) The reference DC with the phase-velocity and uncertainty and the synthetic accepted DCs from the Monte Carlo inversion. (b) The accepted VS models from the Monte Carlo inversion. (c) The accepted VSZ models from the Monte Carlo inversion. In black, the reference time-average VS (d) Estimated reference W/D relationship. The coloured W/D relationships are the synthetic ones, each with constant Poisson's ratio, used for apparent Poisson's ratio estimation. (e) The estimated reference apparent Poisson's ratio.
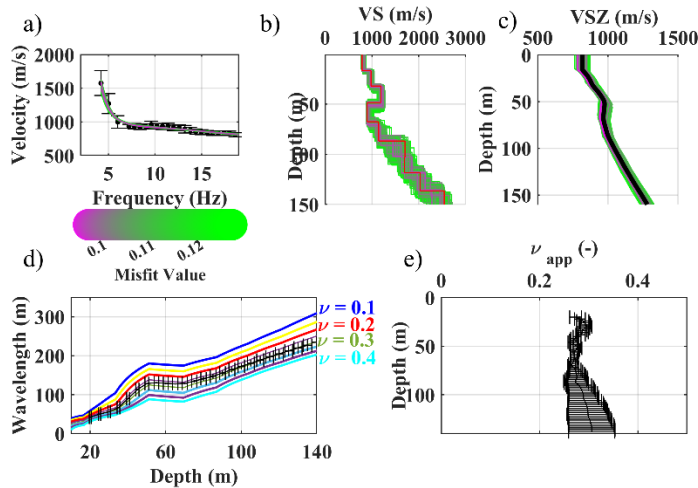
Figure 7: The steps of estimating the reference W/D relationship and apparent Poisson's ratio for cluster B. (a) The reference DC with the phase-velocity and uncertainty and the synthetic accepted DCs from the Monte Carlo inversion. (b) The accepted VS models from the Monte Carlo inversion. (c) The accepted VSZ models from the Monte Carlo inversion. In black, the reference time-average VS (d) Estimated reference W/D relationship. The coloured W/D relationships are the synthetic ones, each with constant Poisson's ratio, used for apparent Poisson's ratio estimation. (e) The estimated reference apparent Poisson's ratio.

Using the estimated VS and VP models at the reference location of each cluster (Fig. 8a and b), we obtained Poisson's ratios required by LCI and SWT methods. In Fig. 8c and d, in blue, we show the estimated Poisson's ratio for cluster A and cluster B, respectively.
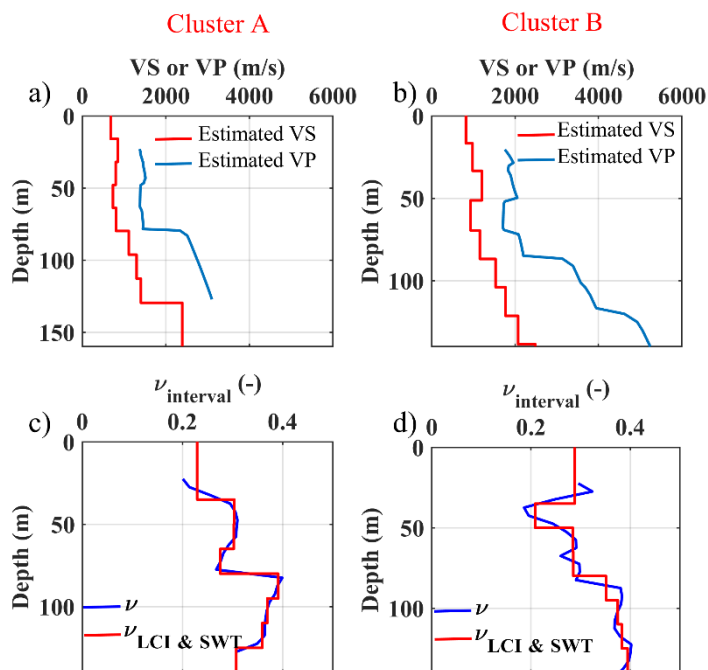
Figure 8: Poisson's ratio estimation for the cluster A and B. (a and b) The estimated VS and VP models corresponding to the reference DC of Clusters A and B. (c and d) In blue, the estimated Poisson's ratio for the cluster A and B. In red, the averaged and extrapolated Poisson's ratio corresponding to the layers of LCI and SWT.

4.3 Results

In Fig. 9, we show several horizontal slices of the estimated VS model averaged over the depth intervals indicated on top of the plots. Similarly, in Fig. 10, we show the horizontal slices of the estimated VP. Both models show a significant velocity contrast between the east and west side of the area, which reduces in the deeper portion of the model.
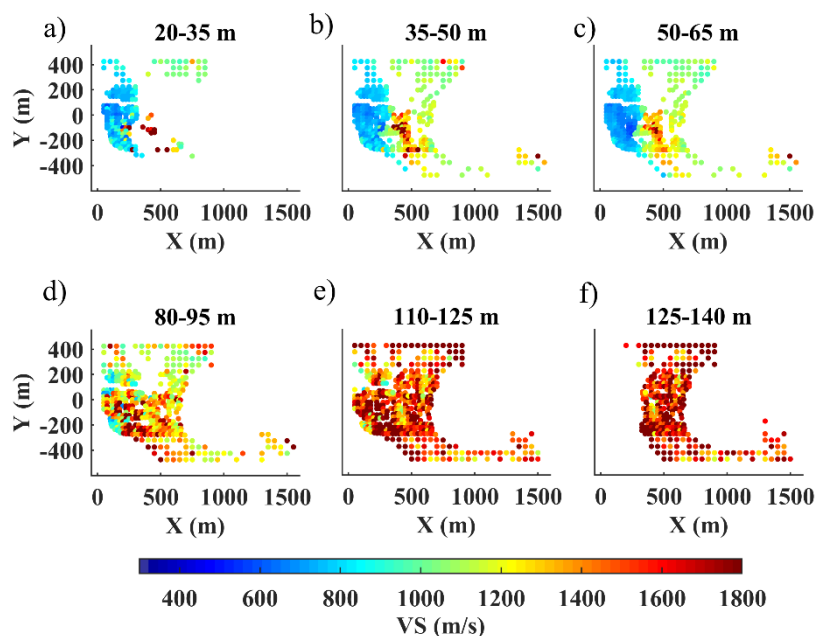
Figure 9: The estimated VS model using the W/D method. (a to f) The horizontal slices at different depth intervals indicated on top of each plot.
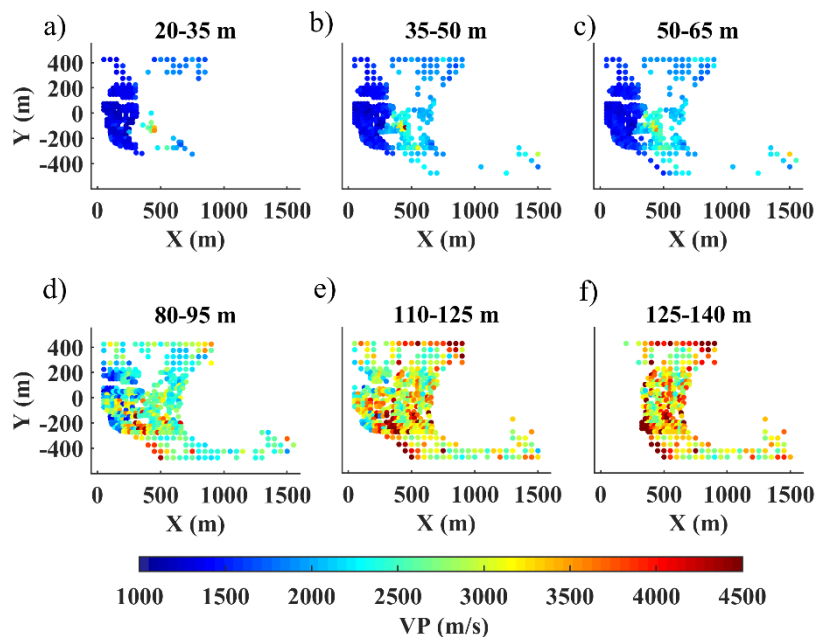
Figure 10: The estimated VP model using the W/D method. (a to f) The horizontal slices at different depth intervals indicated on top of each plot.

5 LCI

5.1 The inputs: multi-channel DCs and initial model

The method's inputs are the multi-channel DCs and the initial models at the location of the local DCs obtained in section 4.1. The initial model is composed of the thickness, density, Poisson's ratio, and VS. We defined the model composed of 9 layers overlying half-space with constant thicknesses of 15 m, except for the first layer which was set 20 m, giving an investigation depth of about 140 m. Estimated Poisson's ratios retrieved from W/D method (blue lines in Fig. 8c and d) were averaged and extrapolated to match the layers of the LCI and SWT. In Fig. 8c and d, in red, we show the adopted Poisson's ratio used for the clusters A and B, respectively. We defined a constant density of 2200 kg/m3, except for the first layer (2000 kg/m3) based on the geological formations in the area.

5.2 Inversion algorithm

The method is a deterministic least-square inversion based on Auken and Christiansen (2004) developed by Boiero (2009) and modified by Khosro Anjom (2021) to support parallel computing. At each iteration the VS and thicknesses are updated, and the VP and density are fixed a priori. All the DCs are inverted contemporarily for a set of 1D models which are tied by lateral constraints between parameters of neighbouring models. The constraints act as spatial regularization, and their strength is defined to avoid both overfitting and over smoothing. We use the data misfit as an indicator for choosing the level of constraints: The inversion with the highest level of constraint that does not impact the DC misfit compared to unconstrained inversion is selected. A thorough description of the method is available in Boiero (2009) and Socco et al. (2009) and the strategy for constraints selection is provided in Boiero and Socco (2010).

5.3 Results

We performed an unconstrained and several laterally constrained inversions to find the optimal level of constraints. We chose a lateral constraint on VS equal to 50 m/s, that was the highest level of constraints that did not significantly impact the inversion's residual misfit. In Fig. 11, we show the horizontal slices of the estimated VS model at various depths corresponding.
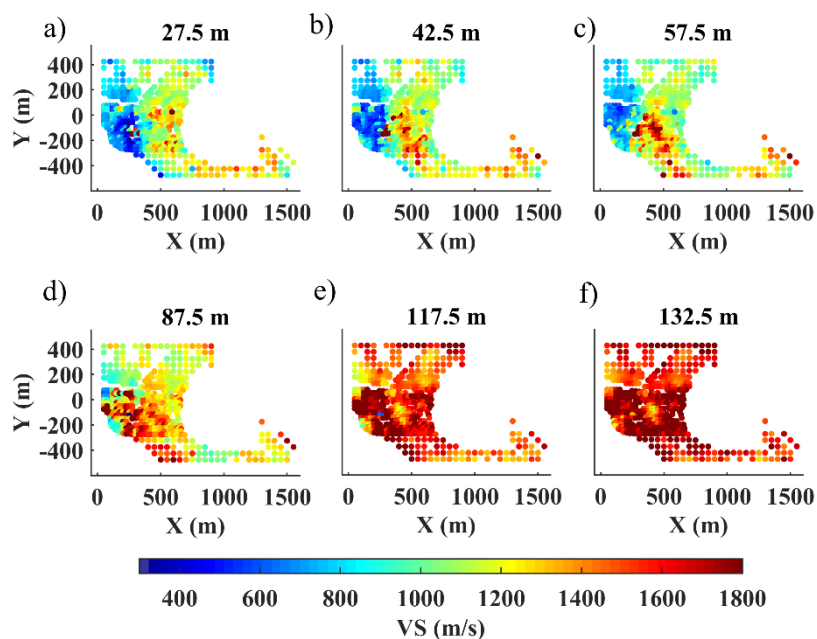
Figure 11: The estimated VS model using the LCI method. (a to f) The horizontal slices at different depths indicated on top of each figure.

6 SWT

6.1 The inputs: two-station DCs and initial model

235   The two-station DCs are estimated using the recordings from receiver couples aligned with a source using interferometry. We use the algorithm developed by Da Col (2019) and modified by Khosro Anjom et al. (2021). First, an automatic search is performed to find the receiver couples aligned with the source at each azimuth angle, considering 1° tolerance for the deviation from a linear path. Then, the traces are narrow band filtered at various frequencies, using zero-phase Gaussian filters. Next, the filtered traces of the receiver couples are cross-correlated and assembled to form the cross-multiplication matrix. We use

240   a 3rd order spline interpolator to convert the cross-multiplication matrix to the frequency-velocity domain. Finally, at each frequency, the phase-velocity is picked as the maximum of the cross-multiplication matrix. To avoid cycle skipping we use as reference the closest multichannel DC, and we automatically pick maxima closest to the reference DCs. To minimize the contamination of the fundamental mode by higher surface-wave modes, we damp the higher mode data using the muting strategy of Khosro Anjom et al. (2019).

245   We applied the SWT to the data from the north of the site only (blue markers in Fig. 2). We performed an automatic search of the receiver couples aligned with sources within 250 m offset, which resulted in 4710 possible receiver couples and source settings. We used the local DCs from the multi-channel analysis (Fig. 5a) as references to locate the correct trend of the path-averaged fundamental mode DCs. We discarded noisy or in inconsistent cross-multiplication matrices and in total, 1301 path-

averaged DCs were estimated. In Fig. 12a and b, we show the estimated path-averaged DCs and the observed azimuthal
250   illumination. The data show uniform coverage with most paths showing angles between 0° to 40° and 140° to 180° angles.
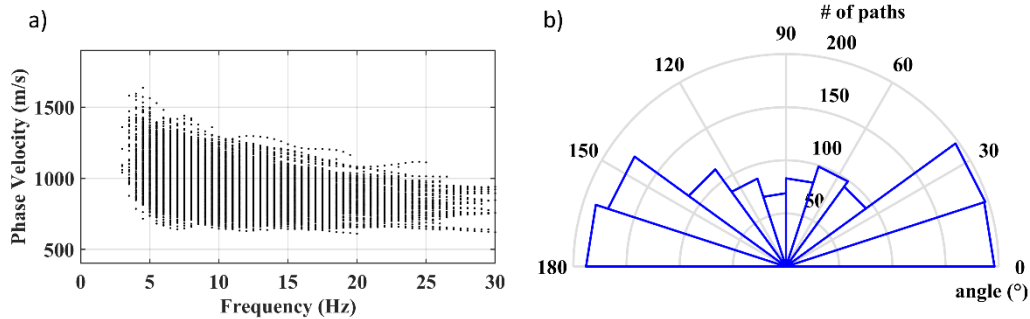
Figure 12: (a) The estimated path-averaged DCs corresponding to north of the data set. (b) The obtained azimuthal illumination with the numbers around the great circle showing the angles and other circles representing the obtained coverage.

In Fig. 13a to f, we show the data coverage within different wavelength ranges, where the colour scale shows the path average
255   phase-velocity. The data exhibit very high coverage for wavelengths between 40 to 220 m, beyond which it decreases
substantially.
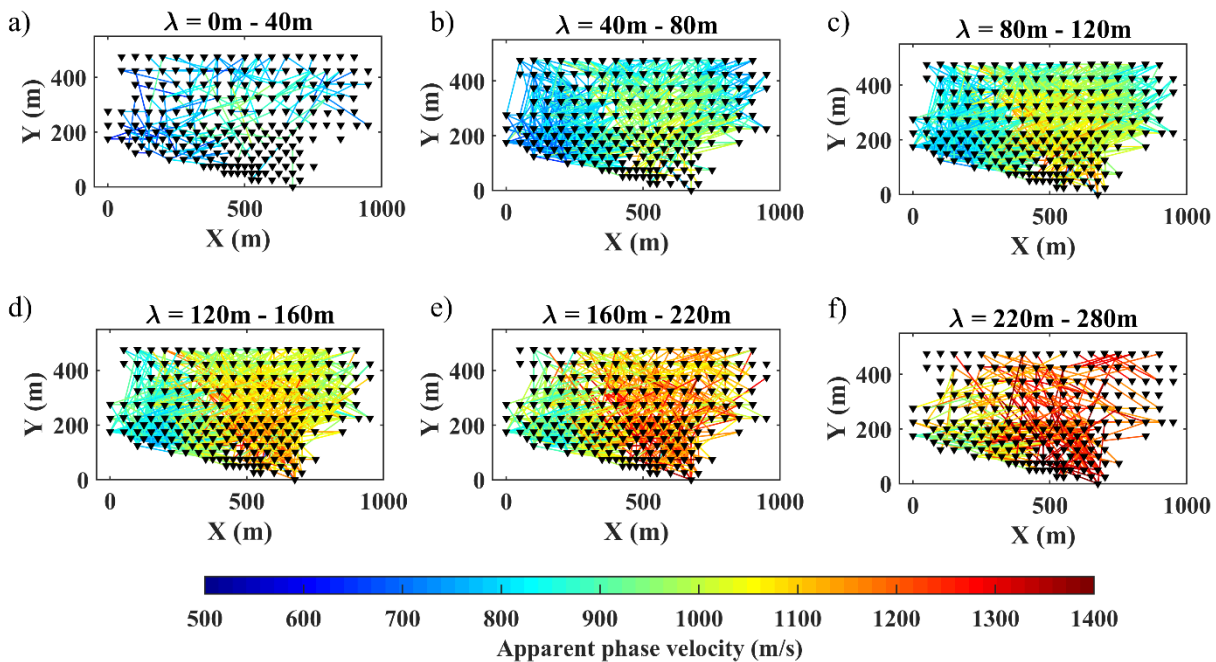
Figure 13: Pseudo-slices of the estimated path-averaged DCs from the north of the site shown within the wavelength ranges: (a) 0 to 40 m.
260   (b) 40 to 80 m. (c) 80 to 120 m. (d) 120 to 160 m. (e) 160 to 220 m. (f) 220 to 280 m.

The parameters of the initial model are the thickness, VS, Poisson's ratio, and density. Given the high data coverage, we defined dense model grid on the considered northern zone, composed of 300 1D models equally distant from each other, aiming at obtaining high resolution model. For the same zone (north), 174 multi-channel DCs and model points were obtained for the W/D and LCI methods, which is almost half of the considered model points for SWT. We considered parameters (VS, VP, density and thicknesses) of the 1D models equal to the ones defined for the LCI (section5.1).

6.2 Inversion algorithm

We use the algorithm developed by Boiero (2009) and modified by Khosro Anjom et al. (2021). An essential part of the SWT is the computation of synthetic path-averaged DCs corresponding to the observed ones. We compute the path-averaged DC from the local DCs of the model points, assuming linear ray-path between the two receivers, using the algorithm developed by Boiero (2009).

Similar to the LCI algorithm, a damped least-least square method is used to iteratively update the model until the minimum misfit between synthetic and observed DCs is reached. The only parameter that updates in the inversion is VS, while the others are fixed a priori. The method allows the implementation of horizontal (lateral) and vertical constraints. We consider the same criteria explained in section 5.2 to select the optimal constraint level.

6.3 Results

In Fig. 14, we show the estimated VS at the different layers, which is in correspondence of the intervals defined for the estimated VS of W/D method (Fig. 8).
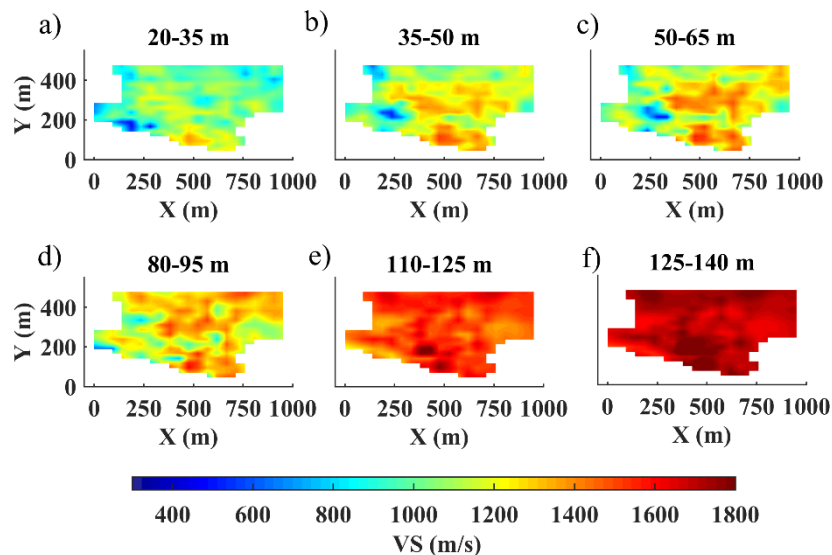
Figure 14: The estimated VS model for the north of the site using the SWT method. (a to f) The horizontal slices at different layers indicated on top of each figure.

7 Discussion

We showed the application of three surface-wave methods for VS model estimation, out of which, the W/D and LCI methods provided the velocity models at the location of DCs, both in the northern zone (174 locations) and southern zone (371 locations). The SWT was applied only to the northern zone, which provided the VS models at 300 defined model points. The

285 W/D method provided continuous velocities in depth, while the SWT and LCI provided layered models. Although we defined similar reference models for the LCI and SWT methods, the LCI was set to also update the thicknesses at each iteration, leading to different parameterization in depth compared to SWT. Here, we further analyse the results in terms of vertical resolution, spatial resolution, differences of the estimated models and computational efficiency of each method.

In Fig. 15, we show the wavelength distribution of the estimated multi-channel DCs in blue that shows dense data sampling

290 up to 300 m of wavelength, suggesting good vertical resolution also in deeper portions. These DCs were obtained from the recordings of receivers spread over a square window of 100×100 m^2. The receiver selection square was shifted by one receiver spacing (50 m in the north and 25 m in the south), which can be considered as the spatial resolution of the multi-channel DC data.
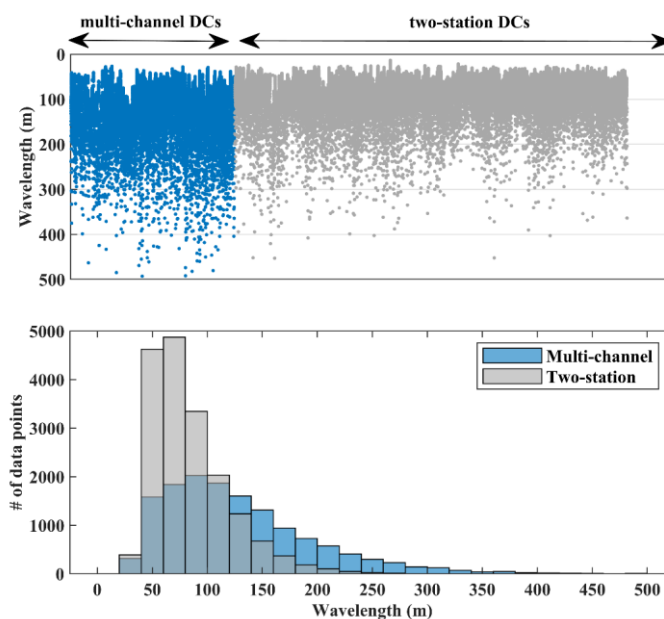
295 **Figure 15:** Comparison between the wavelength distributions of the multichannel and two-station dispersion data. (Top) The distribution of the wavelength shown separately for each estimated DC. (Bottom) The histogram showing the wavelength distribution of all DCs within 20 m wavelength bins.

In Fig. 15, in grey, we also show the wavelength distribution of the estimated two-station DCs. Even though the total number of DCs from two-station analysis (1301) is far more than multi-channel ones (545), the large wavelength datapoints (>120 m)

300 are sparser than the ones obtained with the multi-channel analysis (Fig. 15), mainly due to low signal-to-noise ratio of the cross-multiplication matrices in low frequencies. This shows that multi-channel DC analysis provides better resolution in depth

compared to the two-station method. To mitigate this issue that prevents the estimation of the deepest portion of the model in scheme of SWT, we employed the wavelength-based weighting system developed by Khosro Anjom et al. (2021), to increase the score of large-wavelength data points in the tomographic inversion, aiming at enhancing the resolution in depth. We

305   performed a checkerboard test to evaluate horizontal and vertical resolution of the SWT. We perturbed the estimated VS model from SWT method (Fig. 14) by 8% negatively and positively which alternated every two layers (Fig. 16a and b). In Fig.16c to f, we show the results of the inversion at various layers. The 50×50 m^2 perturbations were well-recovered up to depth of 50 m (Fig. 16c and d), providing similar spatial resolution compared to LCI and W/D methods. The resolution slightly decreases towards the deepest portion of the model (Fig. 16e and f), especially in the northern part where long-wavelength data are

310   lacking (Fig. 13f).
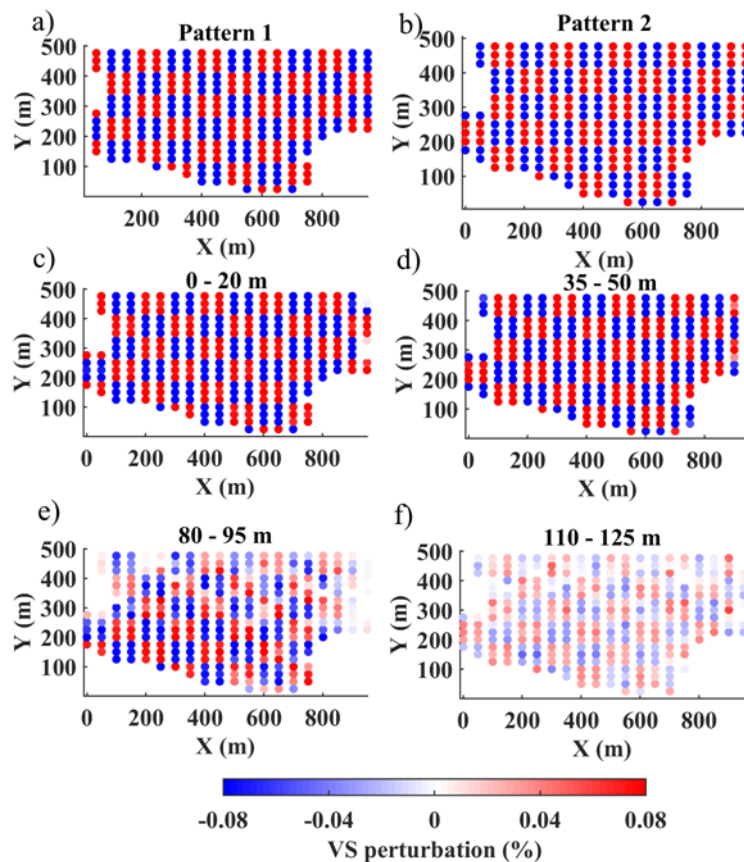
Figure 16: Checkerboard test. (a) The pattern 1 used to perturb VS of layer 1, 2, 5,6, and 9. (b) The pattern used to perturb VS of layer 3,4,7, and 8. (c) 0 to 20 m. (d) 35 to 50 m. (e) 80 to 95 m. (f) 125 to 140 m.

The application of the W/D method to the data set provided both VS and VP models. We considered the estimated Poisson's

315   ratio of the two clusters as prior information in the reference model of the LCI and SWT methods. Now, we use the same Poisson's ratios to transform the VS results of these two methods to VP models. We also linearly interpolate the VS and VP results from all three methods to obtain the velocity models at common voxels of $10 \times 10 \times 0.1$ m^3 within x, y, and z (depth)

directions, respectively. In Fig. 17, we compare the retrieved pseudo 3-D VS and VP models from the three methods at various

iso-surfaces. Very similar trend of variations for VS (left panels) and VP (right panels) are obtained from the application of

320   the methods, and they all depict a significant variation between the east and west side of the site.
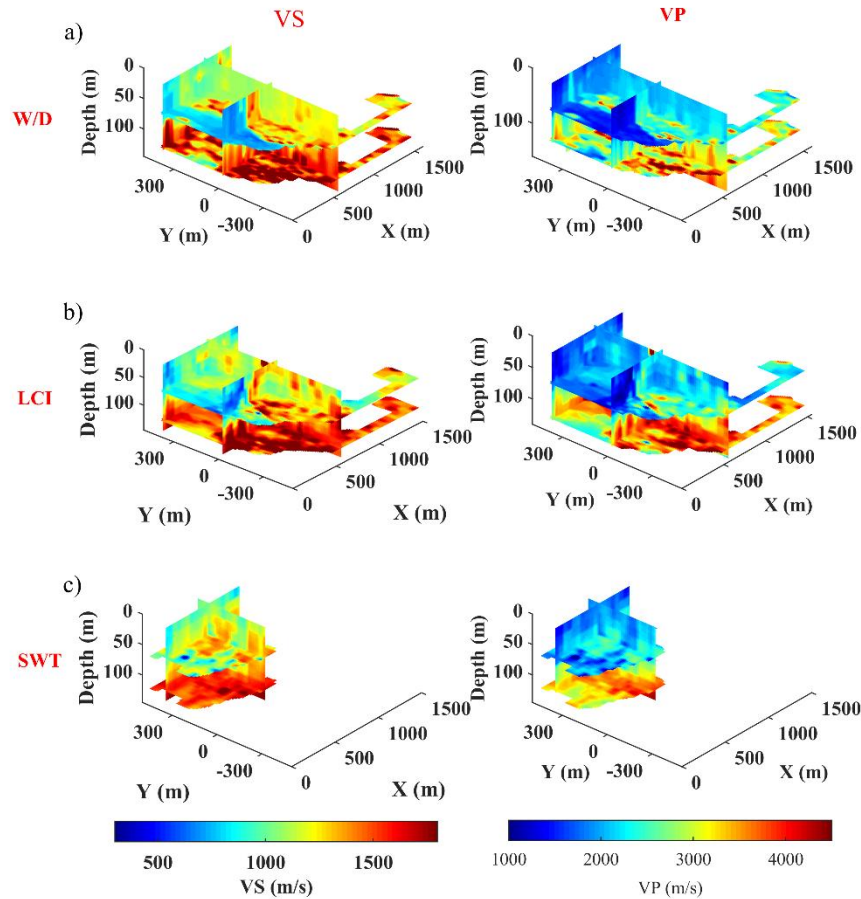
Figure 17: Iso-surfaces of the estimated VS models (left panel) and VP models (right panels) using: (a) W/D, (b) LCI, and (c) SWT methods. The sections are at plains x= 600 m, y =0, and 400 m, and depth = 70, and 125 m.

To compare the estimated models from each method quantitatively, we compute the difference between estimated VS and VP

325   of every two methods separately, as:

$$\varepsilon(i,j,k) = 2 \times \left[\frac{V(i,j,k)_{method.1} - V(i,j,k)_{method.2}}{V(i,j,k)_{method.1} + V(i,j,k)_{method.2}} \right], \tag{1}$$

where i, j, and k are the indices of the voxels in x, y, and z (depth) directions, respectively, and V is the velocity. In Fig.

18, we show the boxplots of the differences compartmentalized within different depth intervals. The box plot is defined by

three lines showing the 25th percentile, median and 75th percentile of the residual's distribution, and whisker lines extending

330   from the box's edges up to 1.5 times the distance between the edges of the box. The rest of the data are considered as outliers

and are shown with "+". The boxplots in Fig. 18 are computed for depths between 20 and 140 m, except for the VS comparison of the LCI and SWT (Fig. 18e), which also includes the first 20 m. This is due to the lack of short wavelength data for the W/D method. The significant registered differences registered of the outliers (red "+") are mainly caused by the methods' different parameterization in depth.

335   The difference between the estimated VS and VP from W/D and LCI methods are small and uniform within different depth ranges (Fig. 18a). Nevertheless, for the deepest layers, a slight over-estimation of the VP from the LCI method is registered compared to the VP from W/D technique (right panel in Fig. 18a). The differences are increased in depth when the VS and VP of the W/D and SWT methods are compared (Fig. 18b). The differences obtained for the estimated VS from the LCI and SWT methods (Fig. 18c) are very similar to the ones observed for the VP, since the VP models of both methods were obtained from

340   the estimated VS and same a priori Poisson's ratios; the differences are mainly less than 5%.
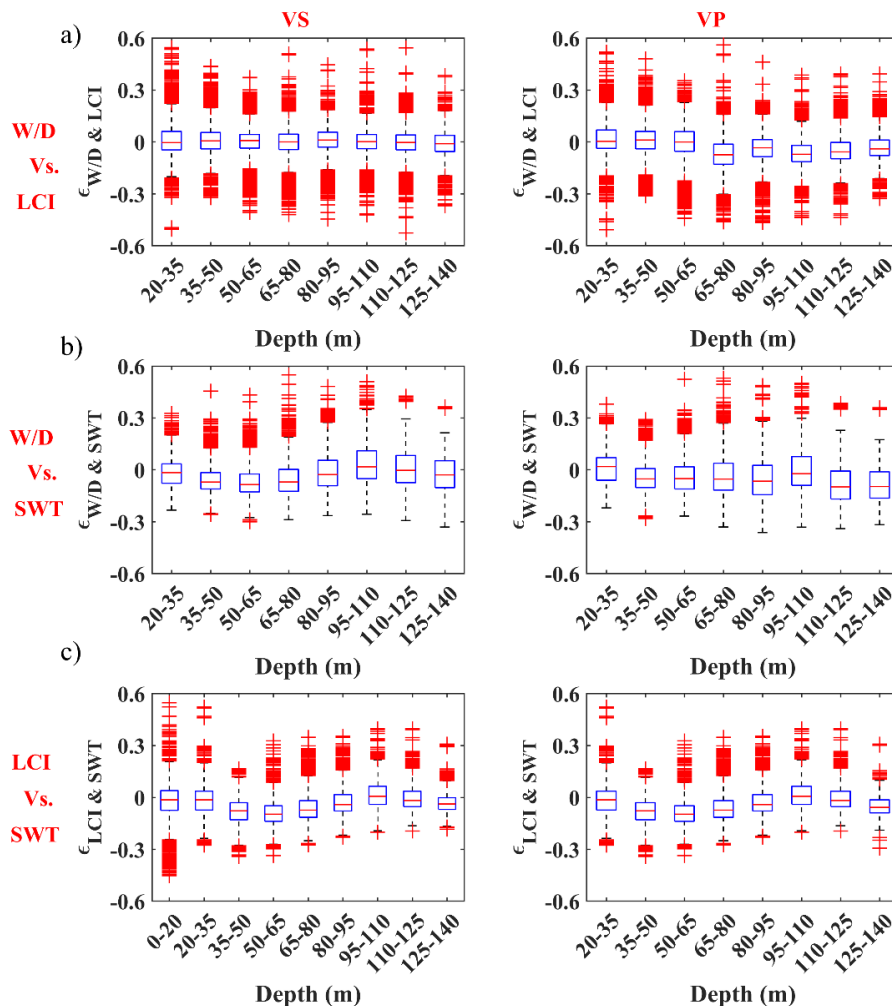
Figure 18: The difference between the VS (left panel) and VP (right panel) models obtained from the three methods computed using equation (1). The differences between the models obtained from: (a) W/D and LCI, (b) W/D and SWT, and (c) LCI and SWT.

We compute the total differences between the estimated models of every two methods as:

$$\varepsilon_{tot} = \left[\frac{1}{n.q}\sum_{j=1}^{q}\sum_{i=1}^{n}\left|\frac{1}{m}\sum_{k=1}^{m}\varepsilon(i,j,k)\right|\right]\times 100,$$

(2)

where m, n, and q are the overall number of voxels in z (depth), x, and y directions, respectively. In Table 2, we report

the values of the total differences obtained by comparing the models from the three methods.

Table 2: The total difference between the estimated VS and VP models obtained from the application of W/D, LCI, and SWT methods.

Total difference	ε_{tot} (VS)	ε_{tot} (VP)
WD vs. LCI	3.3%	4.67%
WD vs. SWT	6%	7.06%
LCI vs. SWT	4.74%	4.52%

In Table 3, we provide the approximated computational costs for each part of the three methods. The most time-consuming

step of all methods is the DC estimation, which also involves expert user intervention. Compared to W/D and LCI, the SWT

usually requires more DCs to reach adequate data coverage for the tomographic inversion. We estimated 1301 DCs for SWT

applied to the north of the site, whereas only 174 DCs were estimated for the application of the W/D and LCI methods to the

same zone. The W/D relationship and Poisson's ratio estimation is a common stage for all three methods. The inversion running

times (for LCI and SWT) given in Table 3 are for a single inversion trial using 10 CPU cores. Usually, in addition to an

unconstrained inversion, several constrained inversions are performed to reach a satisfactory model in scheme of SWT and

LCI methods, whereas the W/D method can be applied faster and is efficient for processing large-scale data sets.

Table 3: The approximated computational costs for each method.

	Processing (DC estimation)	W/D relationship and Poisson's ratio estimation	Model estimation
W/D	1 min/DC	24 hrs	5 s/1D model
LCI	1 min/DC	24 hrs	5 hrs
SWT	1 min/DC	24 hrs	48 hrs

In Fig. 19, we show the geological map superimposed with the satellite view of the area and with the horizontal slice of the estimated VP model from W/D corresponding to the depth between 35-50 m. The two diagonal and vertical faults at the north-west of the investigated area separate the east from the west sides. In the region between the two faults, a gap within the estimated model from the W/D method is observed: The scattering and complex propagation of surface-waves the passes

365   through these discontinuities resulted in inconsistencies in the spectrum that prevented the estimation of reliable DCs. The west of the area is characterized by loose materials from recent deposits (outcrop 5 in Fig. 19). The rest of the region is known for stiffer materials, composed of limestone and marl. The estimated VP also shows a higher velocity in the eastern region. The fastest VP is registered in the correspondence of the Sparnecian formation (outcrop 4 in Fig. 19).
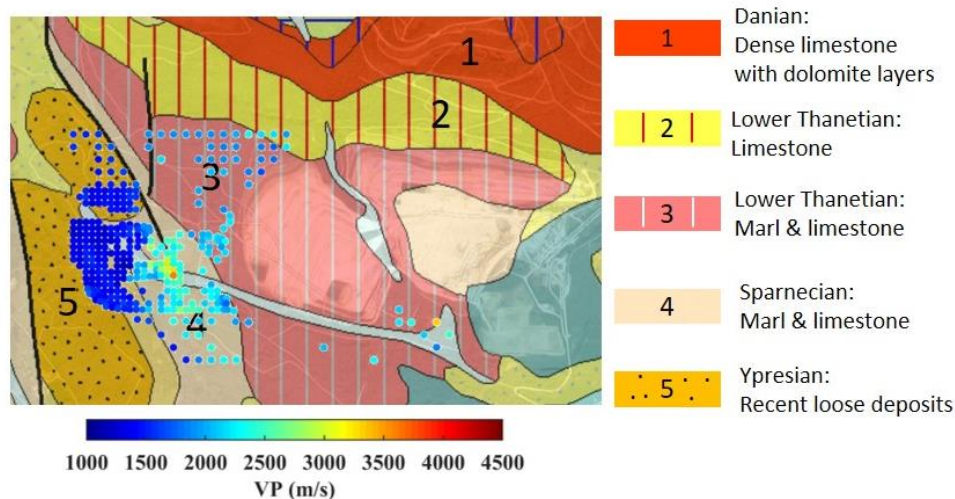
370   **Figure 19:** The geological map of the site, obtained from French Geological Survey (© BRGM - www.infoterre.brgm.fr), superimposed with the area's satellite view (© Google Earth) and the estimated VP corresponding to depth 35-50 m using the W/D method.

8 Conclusions

We showed the application of three surface-wave methods, W/D, LCI, and SWT, to a large test data set from a stiff site to estimate both VS and VP models. The W/D and LCI methods were applied to both zones outside the mining pits, while SWT

375   application was limited to the north of the site. We used the W/D method to estimate a priori Poisson's ratios required for the LCI and SWT methods. The estimated VS and VP models from the three methods were less than 6% and 7.1% different, respectively. The retrieved lateral variation by the methods showed good similarity with the geological information available for the site. The most time-consuming part of the methods are the dispersion curve pickings, especially for the SWT method which requires more DC to reach an adequate data coverage compared to the other two methods. As a result, the automation

380   of the DC picking can be considered a great breakthrough in industrialization of these methods, which enables their fast applications to even larger data sets than the one used in this paper.

Code and data availability. The data are licensed to Politecnico di Torino that allows research activities conducted only by
Politecnico di Torino. As a result, the data cannot be made publicly available. The code for the three surface-wave methods
were developed in other projects. Nevertheless, the code for W/D data transformation method may be available by contacting
the corresponding author.

Author contributions. FKA worked on the application of the methods to the data set with supervision of FA and LVS. FKH
wrote the original paper draft, with the contribution and revisions of FA and LVS.

Competing interests. The contact author declares that neither him nor his co-authors have any competing interests.

Acknowledgements

We would like to thank Gallego Technic Geophysics for licensing the field data. The first author would like to thank
TotalEnergies for supporting his PhD during which this study was carried out.

References

Auken, E. and Christiansen, A. V.: Layered and laterally constrained 2D inversion of resistivity data, Geophysics, 69, 752–
761, https://doi.org/10.1190/1.1759461, 2004.

Auken, E., Christiansen, A. V., Jacobsen, B. H., Foged, N., and Sorensen, K. I.: Piecewise 1D laterally constrained inversion
of resistivity data, Geophys. Prospect., 53, 497–506, https://doi.org/10.1111/j.1365-2478.2005.00486.x, 2005.

Badal, J., Chen, Y., Chourak, M., and Stankiewicz, J.: S-wave velocity images of the Dead Sea Basin provided by ambient
seismic noise, J. Asian Earth Sci., 75, 26–35, https://doi.org/10.1016/j.jseaes.2013.06.017, 2013.

Bao, X., Song, X., and Li, J.: High-resolution lithospheric structure beneath Mainland China from ambient noise and
earthquake surface-wave tomography, Earth Planet. Sci. Lett., 417, 132–141, https://doi.org/10.1016/j.epsl.2015.02.024,
2015.

Beaty, K. S., Schmitt, D. R., and Sacchi, M.: Simulated annealing inversion of multimode Rayleigh wave dispersion curves
for geological structure, Geophys. J. Int., 151, 622–631, https://doi.org/10.1046/j.1365-246X.2002.01809.x, 2002.

Blonk, B. and Herman, G. C.: Inverse scattering of surface waves: A new look at surface Consistency, Geophysics, 59, 963–
972, https://doi.org/10.1190/1.1443656, 1994.

Boiero, D. and Socco, L.V.: Retrieving lateral variations from surface wave dispersion curves, Geophysical Prospecting, 58,
977-996, https://doi.org/10.1111/j.1365-2478.2010.00877.x, 2010.

Boiero, D.: Surface wave analysis for building shear wave velocity models, Ph.D. thesis, Politecnico di Torino, 233 pp., 2009.

Boschi, L., and Ekström, G.: New images of the Earth's upper mantle from measurements of surface wave phase-velocity
415   anomalies: J. Geophys. Res. Solid Earth, 107, 1-14, https://doi.org/10.1029/2000JB000059, 2002.

Comina, C., Foti, S., Boiero, D., and Socco, L. V.: Reliability of VS,30 evaluation from surface-wave tests, J. Geotech.
    Geoenviron. Eng., 137, 579–586, https://doi.org/10.1061/(asce)gt.1943-5606.0000452, 2011.

Da Col, F., Papadopoulou, M., Koivisto, E., Sito, Ł., Savolainen, M., and Socco, L. V.: Application of surface-wave
    tomography to mineral exploration: a case study from Siilinjärvi, Finland, Geophys. Prospect., 68, 254–269,
420   https://doi.org/10.1111/1365-2478.12903, 2020.

Ernst, F. E., Herman, G. C., and Ditzel, A.: Removal of scattered guided waves from seismic data, Geophysics, 67, 1240–
    1248, https://doi.org/10.1190/1.1500386, 2002.

Fang, H., Yao, H., Zhang, H., Huang, Y.-C., and van der Hilst, R. D.: Direct inversion of surface wave dispersion for three-
    dimensional shallow crustal structure based on ray tracing: methodology and application, Geophys. J. Int., 201, 1251–
425   1263, https://doi.org/10.1093/gji/ggv080, 2015.

Feng, S., Sugiyama, T., and Yamanaka, H.: Effectiveness of multi-mode surface wave inversion in shallow engineering site
    investigations, Explor. geophys., 36, 26–33, https://doi.org/10.1071/eg05026, 2005.

Foti, S., Lai, C. G., Rix, G. J., and Strobbia, C.: Surface wave methods for near-surface site characterization, 1st ed., CRC
    Press, London, England, 2017.

430 Garofalo, F., Foti, S., Hollender, F., Bard, P. Y., Cornou, C., Cox, B. R., Dechamp, A., Ohrnberger, M., Perron, V., Sicilia,
    D., Teague, D., and Vergniault, C.: InterPACIFIC project: Comparison of invasive and non-invasive methods for seismic
    site characterization. Part II: Inter-comparison between surface-wave and borehole methods, Soil Dyn. Earthq. Eng., 82,
    241–254, https://doi.org/10.1016/j.soildyn.2015.12.009, 2016.

Halliday, D. F., Curtis, A., Vermeer, P., Strobbia, C., Glushchenko, A., van Manen, D.-J., and Robertsson, J. O.: Interferometric
435   ground-roll removal: Attenuation of scattered surface waves in single-sensor data, Geophysics, 75, SA15–SA25,
    https://doi.org/10.1190/1.3360948, 2010.

Karimpour, M.: processing workflow for estimation of dispersion curves from seismic data and QC = Extraction of Dispersion
    Curves from Field Data, MSc thesis, Politecnico di Torino, 71 pp., 2018.

Karimpour, M., Slob, E., Socco, L.V.: Comparison of straight-ray and curved-ray surface wave tomography approaches in
440   near-surface studies, Solid Earth, 13, 1569-1583, https://doi.org/10.5194/se-13-1569-2022, 2022.

Kennett, B. L. N. and Yoshizawa, K.: A reappraisal of regional surface wave tomography, Geophys. J. Int., 150, 37–44,
    https://doi.org/10.1046/j.1365-246x.2002.01682.x, 2002.

Khosro Anjom, F.: S-wave and P-wave velocity model estimation from surface waves, Ph.D. thesis, Politecnico di Torino, 165
    pp., 2021.

445 Khosro Anjom, F., Teodor, D., Comina, C., Brossier, R., Virieux, J., and Socco, L. V.: Full-waveform matching of VP and
    VS models from surface waves, Geophys. J. Int., 218, 1873–1891, https://doi.org/10.1093/gji/ggz279, 2019.

Khosro Anjom, F., Browaeys, T. J., and Socco, L. V.: Multimodal surface-wave tomography to obtain S- and P-wave velocities applied to the recordings of unmanned aerial vehicle deployed sensors, Geophysics, 86, R399–R412, https://doi.org/10.1190/geo2020-0703.1, 2021.

450 Khosro Anjom, F., Arabi, A., Socco, L.V. and Comina, C.: Application of a method to determine S and P wave velocities from surface waves data analysis in presence of sharp lateral variations, 36th GNGTS national convention, 632-635, https://hdl.handle.net/11583/2740539, 2017.

Lai, C.G.: Simultaneous inversion of Rayleigh phase-velocity and attenuation for near-surface site, Ph.D. thesis, Georgia Institute of Technology, 1998

455 Lys, P.-O., Elder, K., Archer, J., and the METIS Team: METIS, a disruptive R&D project to revolutionize land seismic acquisition, in: RDPETRO 2018: Research and Development Petroleum Conference and Exhibition, Abu Dhabi, UAE, 9-10 May 2018, 2018.

Mari, J. L.: Estimation of static corrections for shear-wave profiling using the dispersion properties of Love waves, Geophysics, 49, 1169–1179, https://doi.org/10.1190/1.1441746, 1984.

460 Mordret, A., Landès, M., Shapiro, N. M., Singh, S. C., and Roux, P.: Ambient noise surface wave tomography to determine the shallow shear velocity structure at Valhall: depth inversion with a Neighbourhood Algorithm, Geophys. J. Int., 198, 1514–1525, https://doi.org/10.1093/gji/ggu217, 2014.

Neducza, B.: Stacking of surface waves, Geophysics, 72, 51-58, https://doi.org/10.1190/1.2431635, 2007.

Papadopoulou, M: Surface-wave methods for mineral exploration, Ph.D. thesis, Politecnico di Torino, 2021.

465 Papadopoulou, M., Da Col, F., Mi, B., Bäckström, E., Marsden, P., Brodic, B., Malehmir, A., and Socco, L. V.: Surface-wave analysis for static corrections in mineral exploration: A case study from central Sweden, Geophys. Prospect., 68, 214–231, https://doi.org/10.1111/1365-2478.12895, 2020.

Park, C. B.: ParkSEIS-3D for 3D MASW Surveys, Fast Times, 24, 2019.

Park, C. B., Miller, R. D., and Xia, J.: Imaging dispersion curves of surface waves on multi-channel record, in: SEG Technical
470 Program Expanded Abstracts 1998, 1998.

Picozzi, M., Parolai, S., Bindi, D., and Strollo, A.: Characterization of shallow geology by high-frequency seismic noise tomography, Geophys. J. Int., 176, 164–174, https://doi.org/10.1111/j.1365-246x.2008.03966.x, 2009.

Ritzwoller, M. H., and Levshin, A. L.: Eurasian surface wave tomography: Group velocities, J. Geophys. Res. Solid Earth, 103, 4839-4878, https://doi.org/10.1029/97JB02622, 1998.

475 Roy, S., Stewart, R. R., and Al Dulaijan, K.: S-wave velocity and statics from ground-roll inversion, Lead. Edge, 29, 1250–1257, https://doi.org/10.1190/1.3496915, 2010.

Shapiro, N. M., Campillo, M., Stehly, L., and Ritzwoller, M. H.: High-resolution surface-wave tomography from ambient seismic noise, Science, 307, 1615–1618, https://doi.org/10.1126/science.1108339, 2005.

Socco, L. V. and Boiero, D.: Improved Monte Carlo inversion of surface wave data, Geophys. Prospect., 56, 357–371,
480 https://doi.org/10.1111/j.1365-2478.2007.00678.x, 2008.

Socco, L. V. and Comina, C.: Time-average velocity estimation through surface-wave analysis: Part 2 — P-wave velocity, Geophysics, 82, U61–U73, https://doi.org/10.1190/geo2016-0368.1, 2017.

Socco, L. V., Boiero, D., Foti, S., and Wisén, R.: Laterally constrained inversion of ground roll from seismic reflection records, Geophysics, 74, G35–G45, https://doi.org/10.1190/1.3223636, 2009.

485   Socco, L. V., Boiero, D., Bergamo, P., Garofalo, F., Yao, H., Hilst, R. D. van der, and Da Col, F.: Surface wave tomography to retrieve near surface velocity models, in: SEG Technical Program Expanded Abstracts 2014, 2014.

Socco, L. V., Comina, C., and Khosro Anjom, F.: Time-average velocity estimation through surface-wave analysis: Part 1 — S-wave velocity, Geophysics, 82, U49–U59, https://doi.org/10.1190/geo2016-0367.1, 2017.

Wang, L., Xu, Y., and Luo, Y.: Numerical Investigation of 3D multichannel analysis of surface wave method, J. Appl. Geophy., 490   119, 156–169, https://doi.org/10.1016/j.jappgeo.2015.05.018, 2015.

Wespestad, C. E., Thurber, C. H., Andersen, N. L., Singer, B. S., Cardona, C., Zeng, X., Bennington, N. L., Keranen, K., Peterson, D. E., Cordell, D., Unsworth, M., Miller, C., and Williams-Jones, G.: Magma reservoir below Laguna del Maule volcanic field, Chile, imaged with surface-wave tomography, J. Geophys. Res. Solid Earth, 124, 2858–2872, https://doi.org/10.1029/2018jb016485, 2019.

495   Wisén, R., and Christiansen, V.: Laterally and Mutually Constrained Inversion of Surface Wave Seismic Data and Resistivity Data, J. Env. and Eng. Geophy., 10, 251-262, https://doi.org/10.2113/JEEG10.3.251, 2005.

Wisén, R., Auken, E., and Dahlin, T.: Combination of 1D laterally constrained inversion and 2D smooth inversion of resistivity data with a priori data from boreholes, Near Surf. Geophys., 3, 71–79, https://doi.org/10.3997/1873-0604.2005002, 2005.

Xia, J., Miller, R. D., Park, C. B., Hunter, J. A., Harris, J. B., and Ivanov, J.: Comparing shear-wave velocity profiles inverted 500   from multichannel surface wave with borehole measurements, Soil Dyn. Earthq. Eng., 22, 181–190, https://doi.org/10.1016/s0267-7261(02)00008-8, 2002.

Xia, J., Miller, R. D., Xu, Y., Luo, Y., Chen, C., Liu, J., Ivanov, J., and Zeng, C.: High-frequency Rayleigh-wave method, J. Earth Sci., 20, 563–579, https://doi.org/10.1007/s12583-009-0047-7, 2009.

Yao, H., Beghein, C., and Van Der Hilst, R.: Surface wave array tomography in SE Tibet from ambient seismic noise and two-505   station analysis - II. Crustal and upper-mantle structure, Geophys. J. Int., 173, 205-219, https://doi.org/10.1111/j.1365-246X.2007.03696.x, 2008.